Materials Today: Proceedings xxx (xxxx) xxx

Contents lists available at ScienceDirect

Materials Today: Proceedings

journal homepage: www.elsevier.com/locate/matpr

A hybrid piezoelectric and electrostatic energy harvester for scavenging arterial pulsations

Ihor Sobianin [a], Sotiria D. Psoma [a,*], Antonios Tourlidakis [b]

[a] School of Engineering & Innovation, The Open University, Walton Hall, Milton Keynes MK7 6AA, UK
[b] Department of Mecahnical Engineering, University of Western Macedonia, Kozani 50100, Greece

ARTICLE INFO

Article history:
Available online xxxx

Keywords:
Human energy harvesting
Hybrid harvester
Piezoelectric nanogenerator
Reverse electrowetting on dielectric (REWOD) phenomenon
Computational fluid dynamics (CFD)
Wearable biosensors

ABSTRACT

Implantable and wearable biomedical devices suffer from a limited lifespan of on-board batteries which require change causing physical discomfort. In order to overcome this, various energy harvesters have been developed as the human body possesses several types of energy available for scavenging through appropriately designed energy harvesting devices, while the cardiovascular system in particular represents a constant reliable source of mechanical energy from vibration. Most conventional energy harvesters exploit only a single phenomenon, such piezo- or triboelectricity, thus producing reduced power density. As an improvement, hybridisation of energy harvesters intends to negate this drawback by simultaneously scavenging energy by multiple harvesters. In the present work, the reverse electrowetting on dielectric (REWOD) phenomenon is combined with the piezoelectric effect in a proof-of-concept hybrid harvester for scavenging biomechanical energy from arterial or other type pulsations. A mathematical model of the harvester was developed; and, an investigation using computational fluid dynamics simulations was carried out using the COMSOL Multiphysics software. The effect of the materials of piezoelectric film and geometrical features of the harvester on parameters such as the displacement, the frequency of pulsations and the energy produced were studied. An experimental setup that could model the time-varying pressures and displacements caused from arterial pulsations was designed and the characteristics of the produced piezoelectrical energy were analysed. A comparison between experimental and computational data was carried out demonstrating a good agreement. The dependencies between geometrical parameters and electrical output were determined and recommendations on piezoelectric materials and design solutions were provided.

Selection and peer-review under responsibility of the scientific committee of the International Conferences & Exhibition on Nanotechnologies, Organic Electronics & Nanomedicine-Nanotexnology 2022.

1. Introduction

Continuous monitoring plays a vital role in a timely diagnosis which prevents a wide range of diseases [1]. In modern medical practice, this approach is implemented via wearable biosensors that register any anomalous biomarker deviations [2]. Wearable electronics require a constant energy supply source which results in the inevitable use of batteries which does not only influence dimensions and the overall layout of the sensor, but any time batteries need replacement a gap in the monitoring occurs. Batteries are quite often used in glucose sensors as they represent a reliable and long-lasting source of energy. For instance, the continuous glucose monitoring (CGM) biosensor [3] has a needle that penetrates skin for data collection which means that any time the battery needs to be changed, the patient must go through a painful procedure of taking the sensor in and out while punctuating the skin.

A human body possesses a substantial amount of energy sources that can be utilised to operate low-power electronics [4–9]. This energy can be harvested by exploiting piezoelectric, triboelectric, electromagnetic, electrostatic, biochemical, and solar nanogenerators (NGs). Yet, a hybridisation of several nanogenerators (NGs) is a recent trend that proves to be a fruitful approach [10–12].

In the current paper, a novel design concept is introduced which aims to explore capabilities of an energy harvester that scavenges

* Corresponding author.
E-mail address: Sotiria.Psoma@open.ac.uk (S.D. Psoma).

https://doi.org/10.1016/j.matpr.2023.05.213
2214-7853/
Selection and peer-review under responsibility of the scientific committee of the International Conferences & Exhibition on Nanotechnologies, Organic Electronics & Nanomedicine-Nanotexnology 2022.

Please cite this article as: I. Sobianin, S.D. Psoma and A. Tourlidakis, A hybrid piezoelectric and electrostatic energy harvester for scavenging arterial pulsations, Materials Today: Proceedings, https://doi.org/10.1016/j.matpr.2023.05.213

energy from the time-variation of the arterial blood pressure. Numerous sensing devices [13–15] successfully exploit pulsatile nature of radial artery for both energy harvesting and monitoring biomarkers. The in vivo method employed in such devices harvest energy via piezoelectric films. When a piezoelectric nanogenerator (PENG) is subjected to external mechanical perturbations, electricity is generated [16]. External stimuli can be paired with the reverse electrowetting on dielectric (REWOD) phenomenon which attracted a considerable interest during the last decade [17–20]. When a droplet of conductive liquid is placed between two electrodes, one of which has a dielectric coating, the droplet acts as a variable capacitor when it is subjected to a periodic mechanical force. The periodically applied force induces a change in area where the droplet overlaps with the dielectric coating, and this causes a variation in the capacitance and forces electric current to flow to the load. In the current study, a computational investigation is performed on a prototype harvester which couples these two energies harvesting principles to obtain a novel REWOD-PENG energy harvester at a "proof-of-concept" level. Fig. 1 illustrates a schematic diagram of the operating concept of the proposed prototype hybrid energy harvester with the potential positioning on the arm. Our recommendations are based on the results of a Computational Fluid Dynamics investigation which was performed using the COMSOL Multiphysics software and measured data obtained from an appropriately designed experimental configuration.

2. Simulations

2.1. Working principle of the harvester

The conceptual design of the REWOD-PENG harvester under investigation consists of a 10x10x10 mm domain which is equally filled with an aquatic solution of LiCl and insulating oil as it is illustrated in Fig. 2(a). Both sides of the domain have electrodes coated with a thin 3 μm parylene-N dielectric material and a 10 nm hydrophobic layer. This denotes the REWOD part of the design which is heavily influenced by the Philips electrowetting lens [21]. The top part of the harvester is made of a membrane that allows oil to come in and out of the domain. However, in order to harvest energy, the droplet of LiCl should be allowed to move in order to cause a change in capacity. A 200 μm PVDF piezoelectric nanogenerator is placed in the lower part of the harvester and, when it is pushed upwards by arterial blood pressure, not only generates energy of its own but at the same time it also transfers its kinetic energy to the conductive droplet which in turn fluctuates causing a change in the overlap to occur. The overlap is an area of the dielectric coated electrode that is covered by the droplet at a given moment of time. It is assumed that a 1 V bias voltage is applied to both electrodes for the REWOD system to work as it is shown in Fig. 2(b).

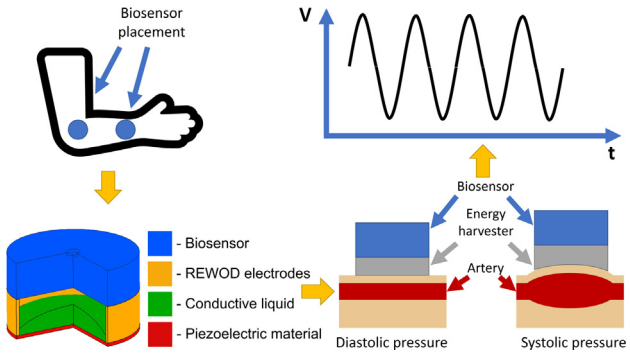

Fig. 1. A schematic diagram of the operating concept of the hybrid energy harvester.

The classic electrowetting on dielectric (EWOD) system modus operandi is based on the fact that the droplet system energy can be altered by an application of external voltage [22]. This, in turn, increases the contact angle (CA) of the droplet with the dielectric film and changes the capacity. The electrowetting contact angle, θ_{ew}, is governed by the Young-Lippman equation:

$$\cos\theta_{ew} = \cos\theta_e + \frac{1}{2\sigma_{12}} C_{areal} V^2 \tag{1}$$

where θ_e is the equilibrium contact angle between two fluids, water and LiCl in the current case, at zero bias, σ_{12} is the surface tension at the interface between the two fluids or the interfacial energy, $C_{areal} = \varepsilon\varepsilon_0/d_f$ is the areal capacitance, ε and ε_0 are the values of permittivity of the dielectric and vacuum permittivity respectively, d_f is the dielectric layer thickness and V is the applied potential difference. The capacitance of the system is given by $C = C_{areal}/A$, where A is the area of the electrode coated with the dielectric film which is in contact with the LiCl droplet. The REWOD system, on the other hand, tends to exploit change in capacitance thus forming a varying capacitor [23]. Based on equation (1), a CA saturation model can be extracted which provides a correlation between the value of the contact angle and the bias voltage as illustrated in Fig. 2c.

The overlap of the REWOD capacitor is determined by the droplet movement inside the domain as it is shown in Fig. 2d. The fluid movement is governed by the continuity and the momentum equations of the fluid motion known as the system of Navier-Stokes equations. By default, COMSOL Multiphysics assumes that the contact angle is static and thus it does not influence the droplet behaviour. The accuracy of the model can be increased if a contact angle hysteresis can be accounted for, thus utilizing a dynamic contact angle (DCA), θ_d. The contact angle is influenced by the velocity of the contact line, U_{cl}, of the fluid–solid interface. If the contact line velocity is greater than zero, then the contact angle is considered as advancing, θ_a. If the velocity is less than zero, the contact angle is considered as receding, θ_d. The relation between the two cases is that $\theta_A > \theta_R$. The advancing contact angle is hydrophobic ($\theta_A \to 0^\circ$), while the receding one is hydrophilic ($\theta_d \to 180^\circ$). The higher the contact line velocity is, the more hydrophobic its advancing angle becomes, while receding becomes more hydrophilic.

Several theories on the implementation of the DCA exist [24], while a significant interest to the DCA model is gathered by the Kistler's law [25] that is expressed as:

$$\theta_d = f_H[C_n + f_H^{-1}(\theta_e)] \tag{2}$$

where $C_n = \mu U_{cl}/\sigma_{12}$ is the capillary number, μ is the dynamic viscosity of the electrolyte, $f_H^{-1}(x)$ is the inverse of Hoffman function which is given as:

$$f_H = arccos\left\{1 - 2tanh\left[5,16\left(\frac{x}{1+1.31x^{0,99}}\right)^{0.706}\right]\right\} \tag{3}$$

Kistler's law allows the development of a model with increased accuracy related to the change of the CA and reduces the requirement of obtaining empirical data for its behaviour. For a given case, the Kistler's law is depicted in Fig. 2e.

Provided that a bias voltage of 1 V is applied, a deviation of CA in response to the contact line velocity due to Kistler law is observed. U_{cl} changes from −0.01 m/s to 0,01 m/s resulting to a change in CA from 139.94° to 140.04°. Further improvements in accuracy can be achieved when the CA hysteresis is corrected by empirical coefficients.

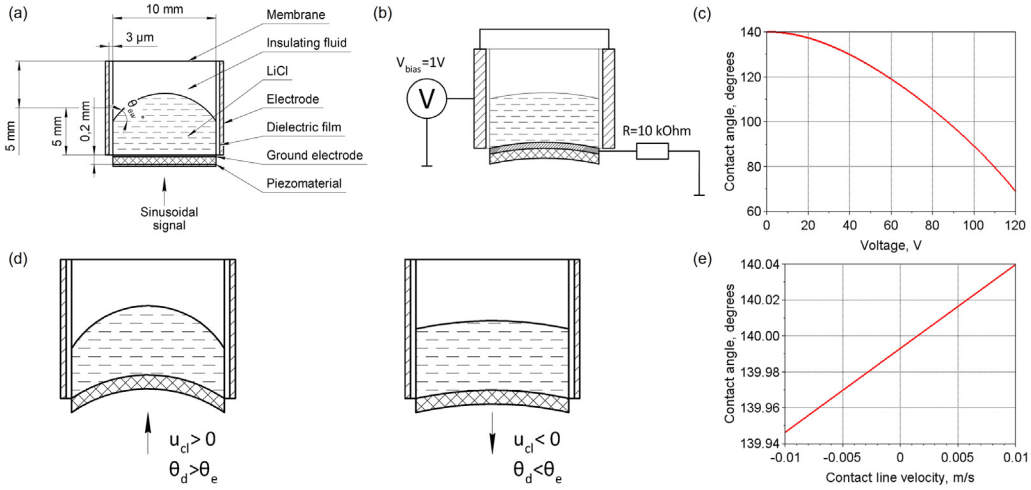

Fig. 2. (a) Concept of the hybrid harvester. (b) Electrical connections of the harvester. (c) Contact Angle saturation model. (d) Kistler's law DCA with 1 V of bias voltage applied. (e) Droplet movement in the hybrid harvester.

2.2. Computational model

The Multiphysics problem at hand requires several physical interfaces coupled together via COMSOL internal functionality. Fig. 3a shows a two-dimensional representation of a chamber where the droplet of LiCl is placed on top of the piezoelectric film and is insulated with the silicon oil. The computational domain consists of three rectangular domains created using the "Geometry" module of COMSOL. Electrodes, dielectric, and hydrophobic coatings are not modeled explicitly but are included through the computation of equation (1).

In most microfluidic systems, the Reynolds number is very small, the flow is laminar and for this reason, the flow behaviour is simulated using the Laminar Flow and Phase Field interfaces that are available in the COMSOL Multiphysics software. The Electrostatics interface is responsible for the calculation of the electric field generated by the action of the piezoelectric nanogenerator (PENG) and therefore only the lower domain is selected for this interface. The piezoelectric domain is allowed to deform due to the blood pressure which is exerted from its lower side. The Solid mechanics interface is applied to the PENG domain in order to calculate the deformation caused to the material due to the application of the external pressure. As such, both sides of the PENG are constrained. The assumed arterial blood pressure has the lowest pressure of 10665 Pa and increases to as high as 15998 Pa with an average frequency of 70 beats per minute. This information was used to simulate an idealised sinusoidal signal for the static pressure time-variation that is applied to the lower boundary of the PENG.

During the course of the computation, the applied pressure is responsible for the deformation of the piezoelectric material which in turn compresses and deforms the liquid domain. The dynamic deformation of solid and liquid domains requires that the computational mesh needs to be generated at every time step in order to discretise the deformed domains. The type of mesh sequence chosen in the current simulations was "Physics-controlled mesh" (Fig. 3b), which means that the mesh was generated automatically by COMSOL Multiphysics to suit all the selected physical interfaces.

The simulations were carried out in a time-varying fashion using Transient analysis with Phase Initialisation for a total duration of 5 s with a time step of 0.01 s which means that a total of 500-time steps were used in the analysis. The interpretation of the computational results is presented in the next section. At every time step the imposed force applied in the lower face of the domain causes the deformation of the piezoelectric layer and this in turn causes the deformation of the interior computational domain.

3. Results and discussions

A computational analysis was performed in order to study the effect of various design parameters on the performance of the energy harvester. Firstly, a baseline case was considered assuming a 10x10 mm computational domain with a piezoelectric layer of 200 μm thickness. Secondly, the effect of the change of the PENG material on the output results was investigated. Thirdly, the thickness of the PENG was varied, and its influence was assessed. In the next study, the effect of the aspect ratio of the computational

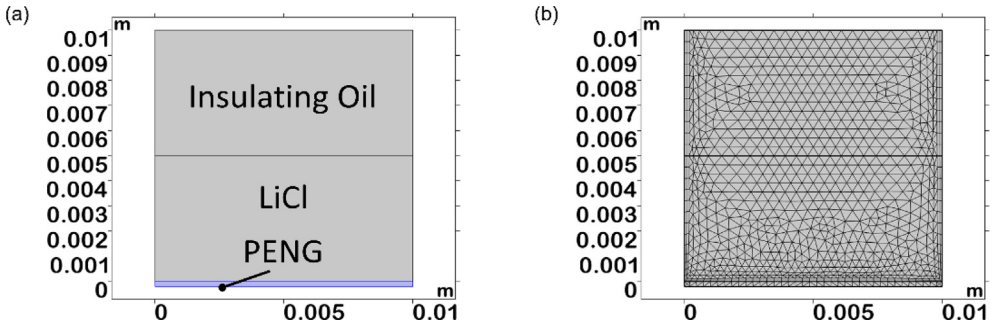

Fig. 3. (a) Computational domain. (b) Generated mesh.

domain through the increase of its width on the electrical output was studied. All simulations were carried out for a duration of 5 s out of which the period of the very first second is ignored in the analysis of the results as during this period a transient process takes place which is strongly affected by the initial conditions which were imposed in a rather arbitrary manner. After this initial period, a repeating pattern is established due to the time-variation of the applied force on the piezoelectric layer.

The first case that was investigated is the baseline REWOD-PENG harvester described in the previous section. A time-varying pressure pulsation was imposed as a boundary condition in the lower surface of the piezoelectric material to simulate the variation of blood pressure in an artery. The dynamic behaviour of how the contact angle varies with time is illustrated in Fig. 4a.

The green line in Fig. 4a is the static contact angle which is defined by the Young-Lippman equation (1), and the blue line shows the time variation of contact angle. It can be compared to the force which is applied to the PENG (Fig. 5b). The characteristics of the overall force that PENG transfers to the liquid is not sufficient to severely increase the contact line velocity. This leads to the conclusion that in such a harvester design, the hysteresis phenomenon only slightly increases the accuracy of the predicted contact angle. The amount of energy harvested from the human body is represented in Fig. 4(c-d). The simulation of PENG provides 9.61 V root mean square (RMS) open circuit voltage (OCV) variation of the output voltage (Fig. 4c), while the capacitance varies from 526 to 528 pF (Fig. 4d). The REWOD energy can be calculated with the method described by Krupenkin and Taylor [26] and is illustrated in Fig. 4e. This method describes the REWOD system as a circuitry with load resistor and varying capacitor where the change in capacitance and the change in energy are approximated. The REWOD system can provide a power of up to 25 nW/mm^2, provided that there is a reliable way of supplying the required bias voltage. The obtained results are comparable to the work presented by Rusev *et al.* [27]. The dynamic flow behaviour can be demonstrated with a plot of the time-varying velocity magnitude of Fig. 4f where two areas of high velocity exist in the chamber: one at the bottom where the PENG is pressed and right at the top. The increase of velocity at the top suggests that this point may be later exploited for energy harvesting purposes.

The influence of three widely used piezoelectric materials, PVDF, ZnO and PZT-4, on the electrical output of the REWOD-PENG harvester were investigated. From the acquired results, it can be deduced that the initially chosen PVDF film presents the highest output ratings in both capacity and piezoelectric voltage output due to the elasticity of the material and the amount of pressure applied to it from the arteries. ZnO and PZT-4 show very similar dynamic behaviour in terms of extracted low electrical output. Highly elastic piezoelectric materials are a preferred choice for this system. The influence of a change in the PENG thickness on the output parameters was also studied. Three different thicknesses of 100 μm, 200 μm (baseline) and 500 μm were investigated. The results show that a decrease in thickness to 100 μm leads to an approximate increase of 6 pF in the maximum capacitance and a slight increase in its amplitude. On the other hand, increase in thickness by 300 μm leads to a decrease in the maximum capacitance to 516 pF and severely reduces its amplitude. PENG output follows the same pattern as decrease in thickness leads to 10.35 V RMS OCV in output, while increasing the thickness has a detrimental effect on the output. The results show that a thickness of 200 μm is an optimum compromise between the performance and the mechanical durability.

Additional studies were carried out and analysed the influence of the aspect ratio of the chamber by changing its width and maintaining the same height. The trend that is discerned in the results is that with an increase in width, the capacity decreases, and the output OCV increases proportionally. Finally, a cylindrical shape chamber was analysed.

Simulated results suggest that harvested energy can be conditioned in two main ways. In both cases the major obstacle is the AC nature of the output signal of both NGs which requires rectification before the energy can be stored. Energy from REWOD and PENG can be independently conditioned via respective active rectification [28] and a diode rectifier or a suitable IC, like LTC3588-1. The drawback of this method is that due to the low output voltage produced by the REWOD component, scavenged energy from the PENG needs to be used for the comparators of the active rectifier [29]. Another way of solving this issue is via using the rectified voltage from PENG to bias REWOD and thus harvesting combined energy output. In this way active rectification is omitted and a compact power management unit for the hybrid harvester is created.

4. Experimental investigation

An experimental setup was designed and built-in order to approximate the model of the harvester, initially exploiting only the piezoelectric effect with a plan to expand it to incorporate

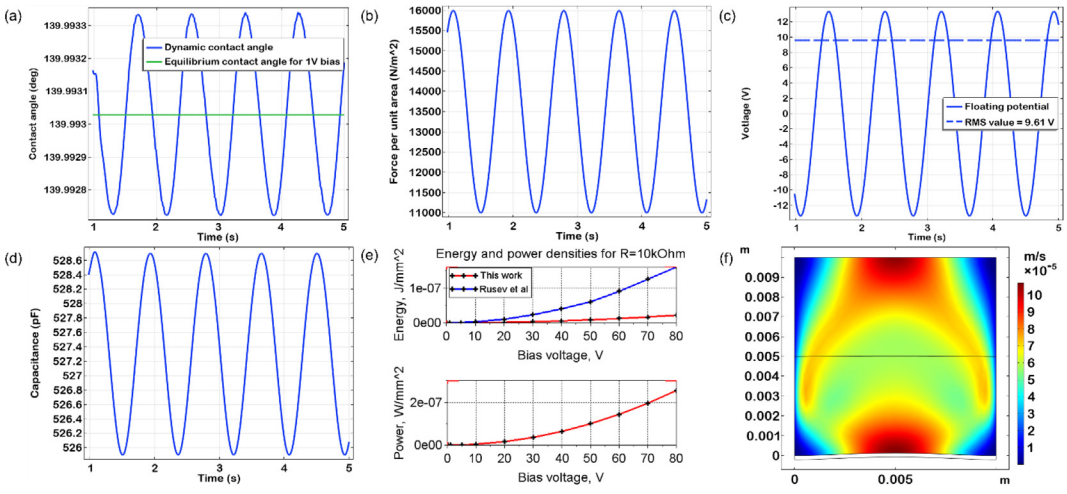

Fig. 4. (a) Contact and dynamic angle. (b) Applied force dynamic variation. (c) PENG output electrical voltage. (d) REWOD capacitance variation. (e) Power ratings comparison. (f) Velocity magnitude.

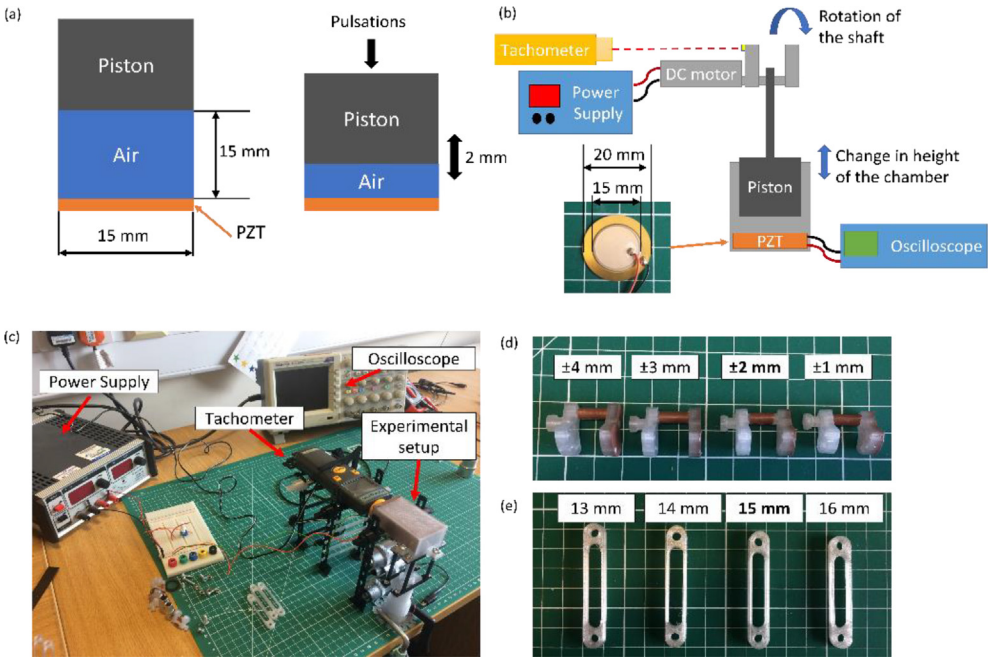

Fig. 5. (a) Pressure chamber structure; (b) Simplified experimental setup diagram; (c) The experimental setup configuration; (d) Variation of the displacement amplitude; (e) Rods for varying the initial chamber height and volume.

the REWOD process. In this case, a chamber filled with air that was compressed by a piston thus causing air compression and expansion which periodically actuated the piezoelectric element. The initial chamber height was 15 mm, and the baseline displacement amplitude of the piston was 2 mm (Fig. 5a).

The experimental setup consisted of the chamber that had a piezoelectric disc (diameter of 20 mm) and a piston that moved upwards and downwards causing pressure variations. The piston was connected to a DC motor via a connecting rod which transformed the rotation of the shaft to linear motion. Each revolution per minute corresponds to a beat per minute (BPM). BPMs were monitored via a tachometer which read optical signal from a reflective tape that was placed on one of the counterweights. The electrical output was measured using an oscilloscope. A simplified form of the setup is presented in Fig. 5b.

The instruments that were used in the experimental setup (Fig. 5c) included a Tektronix 2024C oscilloscope, a 9300-HTK series tachometer from Trumeter and a Farnell LS30-10 power supply. A subminiature 951D series DC motor running at 145 rpm was used to actuate the piston movement. The selected piezoelectric disc was a Murata piezoelectric buzzer (the diaphragm has a diameter of 20 mm and the ceramics surface 15 mm).

For the manufacturing of the parts used in the experimental setup, a natural Ultrafuse® PET was used and all parts were manufactured using a Ultimaker S5 3D printer. The speed of the motor was regulated by changing the power supply voltage. The speed changed from 60 BPMs, which corresponds to ~ 2.1 V, up to 150 BPMs (which corresponds to ~ 5.1 V) with a step of 10 BPMs. Thus, each measurement campaign consisted of recording 10 signals, each corresponding to the respective value of BPM. This process was repeated for 8 times for each value of the parameter under investigation. The obtained spectra of signals were then averaged and plotted using Matlab. Maximum voltage outputs of the obtained spectra of each value of BPM were plotted in a separate graph.

In the experiment, the displacement amplitude (the distance travelled by the piston) and the height of the chamber were varied. A set of 4 counterweights and 4 moving rods were designed. In order to vary piston amplitude, the crank radius was changed from 1 mm to 4 mm with 1 mm step (Fig. 5d). To vary piston chamber height, a set of rods with different length were manufactured varying the baseline height from 13 mm to 16 mm with a 1 mm step (Fig. 5e).

A study of the displacement amplitude was conducted (Fig. 6a-d). The chamber height was constant 15 mm. The results showed an anticipated increase in the output voltage due to increase in actuation frequency. Consequently, the most effective use of the piezoelectric disk can be found at 150 BPM. The variation of the amplitude shows that the longer the piston travel distance is, the higher values of voltage can be observed. The maximum value was 87.29 mV at 4 mm of the displacement amplitude at a speed of 150 BPM (Fig. 6d) and the lowest voltage was 3.55 mV at a displacement amplitude of 1 mm at a speed of 60 BPM (Fig. 6a). A plot of maximum values for each frequency shows a clear increasing trend for the voltage output with both amplitude and frequency (Fig. 6e).

Similarly, the same method was applied to the study of the effect of the chamber height (Fig. 7a-d). The displacement amplitude was constant and equal to 2 mm. However, the final comparison results are quite close to each other, and the largest value can be attributed to the initial chamber height of 15 mm at 150 BPM and this value is equal to 41.26 mV while the lowest value was 3.04 mV and corresponded to 13 mm height at 60 BPM. Overall, the baseline height of 15 mm showed good results throughout the whole frequency range (Fig. 7b) whereas the 16 mm height seemed to show the lowest increase in output with increasing frequency (Fig. 7a). A plot of maximum values shows an increasing trend in output voltage with frequency, however the change in the height does not have a substantial effect on output voltage (Fig. 7e). In order to further investigate the process, a computational analysis was undertaken with the computational domain (Fig. 8a) featuring a matching geometry to the one of experimental setup was designed. It consists of a chamber filled with air where at the bottom of the chamber a brass disc with PZT-5H piezoelectric material is placed (Fig. 8b). The chamber is 17 mm in diameter and 15 mm in height. The top right side of the chamber features an

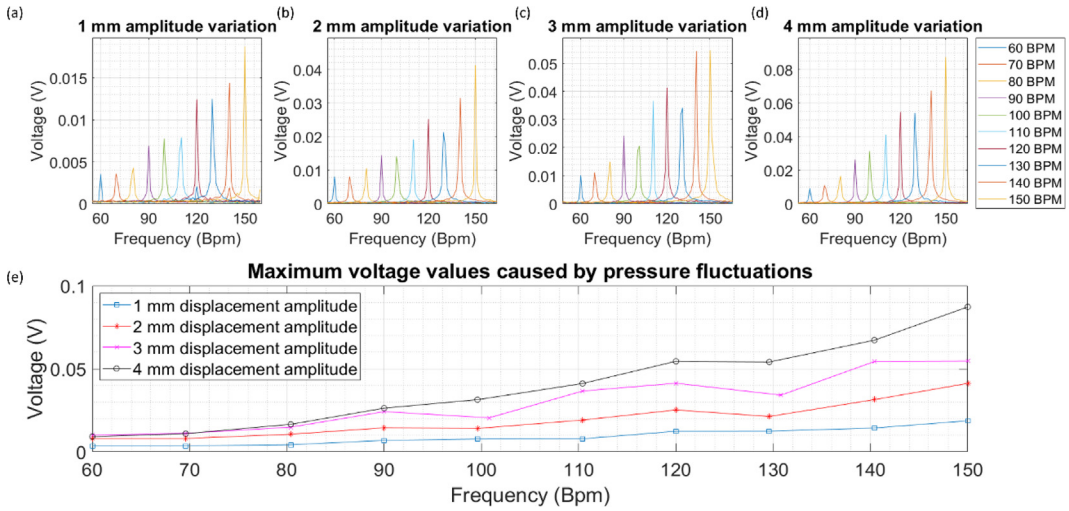

Fig. 6. Amplitude spectra of piezoelectric chamber for (a) 1 mm, (b) 2 mm, (c) 3 mm, (d) 4 mm amplitudes respectively and the maximum voltages of the obtained spectra (e).

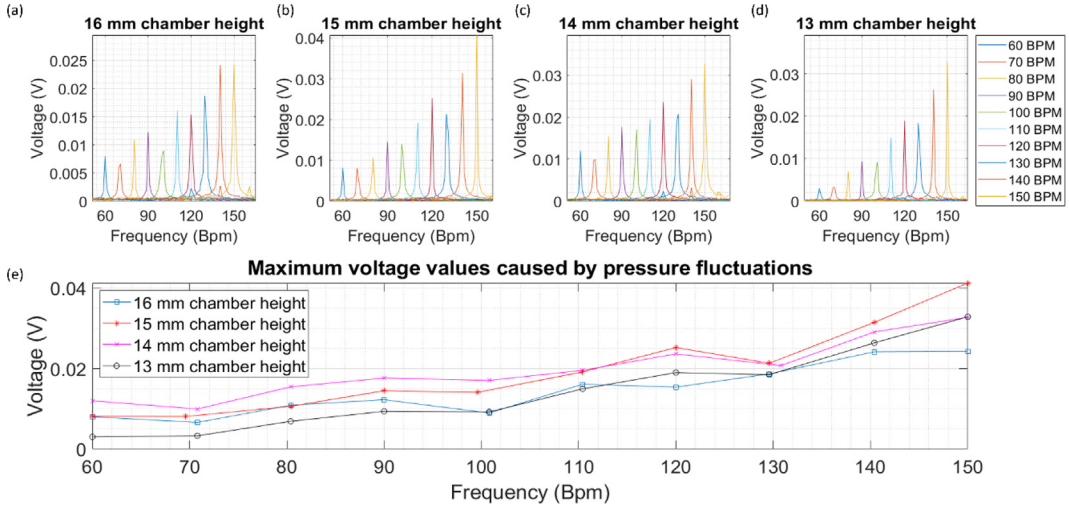

Fig. 7. Amplitude spectra of piezoelectric chamber for (a) 16 mm, (b) 15 mm, (c) 14 mm, (d) 13 mm height respectively and the maximum voltages of the obtained spectra (e).

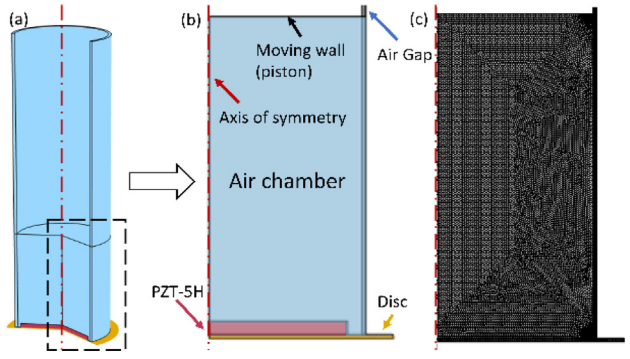

Fig. 8. (a) 3D representation of the computational domain; (b) Computational domain structure; (c) Computational mesh.

air gap which accounts for the non-ideal sealing of the chamber. Its baseline value is 1% of the piston diameter. The movement of the piston is simulated through an Arbitrary Lagrangian Eulerian method (also known as *moving mesh*) to simulate the moving boundary. Since the investigated geometry is cylindrical, the computational domain is made axisymmetric. The computational mesh is generated with "Fine" settings and the air gap channel is constructed with Mapped distribution which has 16 elements in its width and 128 elements in its height (Fig. 8c).

The influence of the air gap was studied by changing its size from 1% to 3% of the piston diameter. The results showed that with the increase of the gap, the output voltage starts to decrease significantly. In particular, even a slight increase in the gap's size from 1% to 1.25%, leads to an almost half output voltage. Yet, if the increase continues, it has a reduced effect after 1.75%. Owing that the exact value of this gap is unknown, its size can be increased or decreased to match the results of the experiment.

The results of the modeling show that the increasing trend of the output voltage as the frequency increases, is the same to that experienced during the experiment. Fig. 9 shows a comparison between the results for the case of 2 mm amplitude variation. The decrease of the output voltage on certain frequencies is attributed to spectral leakage which is inherent to the FFT analysis method. The mismatch between the results can be to the uncertainty about the air gap size. Comparing the simulated and experimental signals at 150 BPM, it can be estimated that the real airgap value is about 1.2% of the piston diameter.

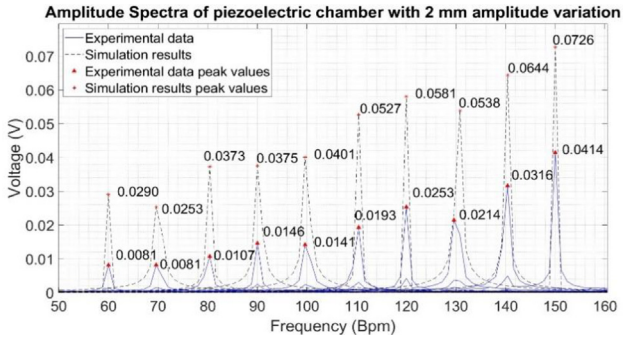

Fig. 9. Comparison between computational and experimental results from the study on the influence of the air gap size.

Pressure contours of the computational domain were plotted at 2 s, 2.24 s, 2.5 s and 2.76 s for the case of 60 BPM frequency and 2 mm amplitude variation (Fig. 10). Figures show that second order processes, such as vortices, are taking place in the chamber during the time when the piston is in its highest and lowest positions, which is seen from the direction of velocity vectors. The pressure varies almost symmetrically between cycles when the piston moves up (Fig. 10b), and down, (Fig. 10c), presenting a maximum of 88.5 Pa and a minimum of −88.5 Pa. Immediately after 2.76 s (Fig. 10d), the next cycle commences which repeats the same processes (Fig. 10a). The obtained plots also capture the electric potential distribution inside the piezoelectric material and the distribution appears to be divided by a parabola that goes from the bottom right corner to the top left corner.

5. Conclusions

In this research paper a "proof-of-concept" REWOD-PENG energy harvester that exploits the pulsatile nature of arteries is proposed. A computational multiphysics model of a conceptual design of the harvester was formulated and subsequently it was used in the development of the mathematical modelling. The COMSOL Multiphysics software was successfully utilised and demonstrated the feasibility of the proposed energy harvesting approach. The calculation of the contact angle is very crucial for the accurate quantification of the contribution of the REWOD phenomenon on the generated energy as compared to the piezoelectric affect. Different geometries were simulated and based on the obtained results a number of engineering recommendations for the REWOD-PENG harvester are proposed. The baseline design that was studied, produced up to 9.61 V RMS OCV from the PENG and the capacitance of the REWOD harvester varied from 526 pF to 528 pF. The PENG from PVDF exhibited the best results in terms of both electric output and elasticity, especially if it is represented by a thin film (<= 200 μm). The simulation showed that the width of the hybrid microfluidic platform should be kept at an optimum level as with its increase, REWOD performance characteristics deteriorate, whereas the PENG output increases. An experimental setup was designed and built-in order to investigate the behaviour of the PENG harvester demonstrating an increased output voltage with increasing frequency. The experimental investigation and results were supported by a parallel computational analysis which aimed towards a better understanding of the process involved. The clearance gap between the piston and the cylinder proved to have a significant inverse influence on the voltage output.

CRediT authorship contribution statement

Ihor Sobianin: Data curation, Investigation, Formal analysis, Validation, Methodology, Visualization, Software, Writing - original draft. **Sotiria D. Psoma:** Conceptualization, Investigation, Methodology, Project administration, Resources; Funding acquisition; Supervision, Validation, Visualization, Writing – review & editing. **Antonios Tourlidakis:** Formal analysis, Investigation, Methodology, Supervision, Validation, Visualization, Writing - review & editing.

Data availability

No data was used for the research described in the article.

Declaration of Competing Interest

The authors declare that they have no known competing financial interests or personal relationships that could have appeared to influence the work reported in this paper.

References

[1] S.S. Gambhir, T.J. Ge, O. Vermesh, R. Spitler, G.E. Gold, Continuous health monitoring: An opportunity for precision health, Sci. Transl. Med. 13 (597) (2021), https://doi.org/10.1126/scitranslmed.abe5383.
[2] J.P.L. Leenen, C. Leerentveld, J.D. Van Dijk, H.L. Van Westreenen, L. Schoonhoven, G.A. Patijn, Current Evidence for Continuous Vital Signs Monitoring by Wearable Wireless Devices in Hospitalized Adults: Systematic Review, J. Med. Internet Res. 22 (6) (2020), https://doi.org/10.2196/18636.
[3] A. Blum, Freestyle Libre Glucose Monitoring System, Clin. Diabetes 36 (2) (2018) 203–204, https://doi.org/10.2337/cd17-0130.
[4] X. Guo, L. Liu, Z. Zhang, S. Gao, T. He, Q. Shi, C. Lee, Technology evolution from micro-scale energy harvesters to nanogenerators, J Micromech. Microeng. 31 (9) (2021) 093002, https://doi.org/10.1088/1361-6439/ac168e.

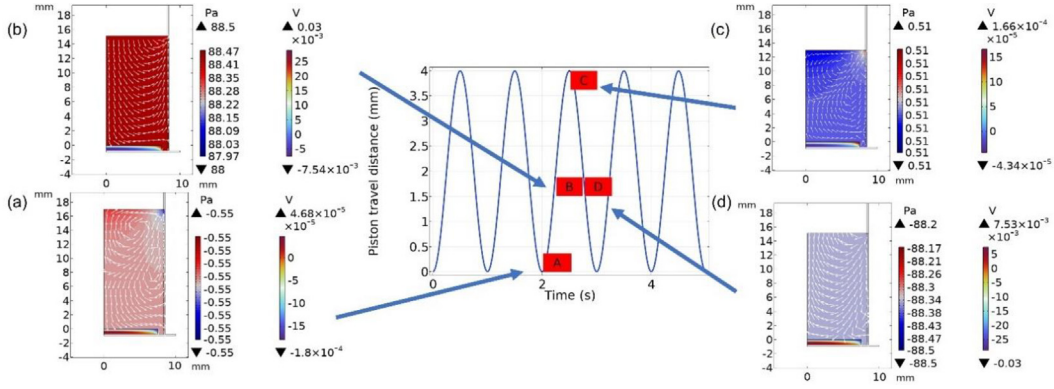

Fig. 10. Pressure contours with velocity vectors and piezoelectric electric potential distribution plotted for 60 BPM at (a) 2 s, (b) 2.24 s, (c) 2.5 and (d) 2.76 s of runtime with arrows pointing towards the exact position of the piston travel distance.

[5] T. He, X. Guo, C. Lee, Flourishing energy harvesters for future body sensor network: from single to multiple energy sources, iScience 24 (1) (2021) 101934. https://doi.org/10.1016/j.isci.2020.101934.
[6] G. Rong, Y. Zheng, M. Sawan, Energy Solutions for Wearable Sensors: A Review, Sensors 21 (11) (2021) 1–23, https://doi.org/10.3390/s21113806.
[7] Y. Song, D. Mukasa, H. Zhang, W. Gao, Self-Powered Wearable Biosensors, Acc. Chem. Res. 2 (3) (2021) 184–197, https://doi.org/10.1021/accountsmr.1c00002.
[8] T. Zhang, T. Yang, M. Zhang, C.R. Bowen, Y. Yang, Recent Progress in Hybridized Nanogenerators for Energy Scavenging, iScience 23 (11) (2020) 101689. https://doi.org/10.1016/j.isci.2020.101689.
[9] I. Sobianin, S.D. Psoma, A. Tourlidakis, Recent advances of energy harvesting from the human body for biomedical applications, Energies 15 (2022) 7959, https://doi.org/10.3390/en15217959.
[10] U. Erturun, A.A. Eisape, S.H. Kang, West JE Energy harvester using piezoelectric nanogenerator and electrostatic generator, Appl. Phys. Lett. 118 (6) (2021) 063902, https://doi.org/10.1063/5.0030302.
[11] R.A. Surmenev, R.V. Chernozem, I.O. Pariy, M.A. Surmeneva, A review on piezo- and pyroelectric responses of flexible nano- and micropatterned polymer surfaces for biomedical sensing and energy harvesting applications, Nano Energy 79 (2021) 105442, https://doi.org/10.1016/j.nanoen.2020.105442.
[12] X. Zhang, B.C. Shiu, T.T. Li, X. Liu, H.T. Ren, Y. Wang, C.W. Lou, J.H. Lin, Photo-thermoelectric nanofiber film based on the synergy of conjugated polymer and light traps for the solar-energy harvesting of textile solar panel, Sol. Energy Mater. Sol. Cells 232 (2021) 111353, https://doi.org/10.1016/j.solmat.2021.111353.
[13] B.H. Moghadam, M. Hasanzadeh, A. Simchi, Self-Powered Wearable Piezoelectric Sensors Based on Polymer Nanofiber–Metal–Organic Framework Nanoparticle Composites for Arterial Pulse Monitoring, ACS Appl. Nano Mater. 3 (9) (2020) 8742–8752, https://doi.org/10.1021/acsanm.0c01551.
[14] M. Wu, Y. Wang, S. Gao, R. Wang, C. Ma, Z. Tang, N. Bao, W. Wu, F. Fan, W. Wu, Solution-synthesized chiral piezoelectric selenium nanowires for wearable self-powered human-integrated monitoring, Nano Energy 56 (2019) 693–699, https://doi.org/10.1016/j.nanoen.2018.12.003.
[15] Z. Yi, J. Huang, Z. Liu, J. Liu, B. Yang, Portable, Wireless Wearable Piezoelectric Arterial Pulse Monitoring System Based on Near-Field Communication Approach, IEEE Electron. Device Lett. 41 (1) (2020) 183–186, https://doi.org/10.1109/LED.2019.2954878.
[16] S.D. Mahapatra, P.C. Mohapatra, A.I. Aria, G. Christie, Y.K. Mishra, S. Hofmann, V.K. Thakur, Piezoelectric Materials for Energy Harvesting and Sensing Applications: Roadmap for Future Smart Materials, Adv. Sci. 8 (17) (2021) 2100864, https://doi.org/10.1002/advs.202100864.
[17] P.R. Adhikari, N.T. Tasneem, R.C. Reid, I. Mahbub, Electrode and electrolyte configurations for low frequency motion energy harvesting based on reverse electrowetting, Sci. Rep. 11 (1) (2021) 5030, https://doi.org/10.1038/s41598-021-84414-3.
[18] F.G. Boroujeni, B. Raissi, S. Jafarabadi-Ashtiani, R. Riahifar, M. Sahba-Yaghmaee, Droplet-based energy harvester considering electrowetting phenomena, Mater. Res. Express 2 (4) (2020) 045028, https://doi.org/10.1088/2631-8695/abce98.
[19] T.H. Hsu, S. Manakasettharn, J.A. Taylor, T. Krupenkin, Bubbler: A Novel Ultra-High Power Density Energy Harvesting Method Based on Reverse Electrowetting, Sci. Rep. 5 (1) (2015) 16537, https://doi.org/10.1038/srep16537.
[20] H. Wu, N. Mendel, S. Van der Ham, L. Shui, G. Zhou, F. Mugele, Charge Trapping-Based Electricity Generator (CTEG): An Ultrarobust and High Efficiency Nanogenerator for Energy Harvesting from Water Droplets, Adv. Mater. 32 (33) (2020) 2001699, https://doi.org/10.1002/adma.202001699.
[21] S. Kuiper, B.H.W. Hendriks, Variable-focus liquid lens for miniature cameras, Appl. Phys. Lett. 85 (7) (2004) 1128–1130, https://doi.org/10.1063/1.1779954.
[22] F. Mugele, J.C. Baret, Electrowetting: from basics to applications, J. Phys.: Condens. Matter. 17 (28) (2005), https://doi.org/10.1088/0953-8984/17/28/R01, R705-R774.
[23] S. Meninger, J. Mur-Miranda, R. Amirtharajah, A. Chandrakasan, J. Lang, Vibration-to-electric energy conversion, IEEE Trans. VLSI Syst. 9 (2001) 64–76, https://doi.org/10.1109/92.920820.
[24] J. Göhl, A. Mark, S. Sasic, F. Edelvik, An immersed boundary based dynamic contact angle framework for handling complex surfaces of mixed wettabilities, Int. J. Multiph Flow 109 (2018) 164–177, https://doi.org/10.1016/j.ijmultiphaseflow.2018.08.001.
[25] M. Andersson, S.B. Beale, W. Lehnert, Dynamic contact angle modeling of droplet reattachment at the gas channel wall in polymer electrolyte fuel cells, eTransportation 1 (100003) (2019), https://doi.org/10.1016/j.etran.2019.100003.
[26] T. Krupenkin, J.A. Taylor, Reverse electrowetting as a new approach to high-power energy harvesting, Nat. Commun. 2 (1) (2011) 448, https://doi.org/10.1038/ncomms1454.
[27] R. Rusev, G. Angelov, K. Angelov, D. Nikolov, A model for reverse electrowetting with cost-effective materials, in: IEEE: 2017 XXVI International Scientific Conference Electronics (ET), 2017, https://doi.org/10.1109/ET.2017.8124371.
[28] C.A. Gong, IC-Based Rectification Circuit Techniques for Biomedical Energy-Harvesting Applications, Micromachines 13 (3) (2022) 411, https://doi.org/10.3390/mi13030411.
[29] A. Ballo, M. Bottaro, A.D. Grasso, A Review of Power Management Integrated Circuits for Ultrasound-Based Energy Harvesting in Implantable Medical Devices, Appl. Sci. 11 (6) (2021) 2487, https://doi.org/10.3390/app11062487.